

The influence of spatial variability in snowmelt and active layer thaw on hillslope drainage for an alpine tundra hillslope

William L. Quinton,^{1*} Robert K. Bemrose,¹ Yinsuo Zhang² and Sean K. Carey²

¹ Cold Regions Research Centre, Wilfrid Laurier University, Waterloo, Canada

² Department of Geography and Environmental Studies, Carleton University, Ottawa, Canada

Abstract:

In alpine tundra, hillslope drainage occurs predominantly below the ground surface, between the relatively impermeable frost table and the water table above it. The saturated hydraulic conductivity decreases by two to three orders of magnitude between the ground surface and the top of the mineral substrate at 0.2–0.3 m depth. Consequently, the rate of sub-surface conveyance from hillslopes strongly depends on the degree of active layer thaw. In addition, although rarely examined, the volume and timing of hillslope drainage and streamflow in alpine tundra are strongly influenced by the spatial pattern of active layer thaw in the runoff-contributing hillslopes. The spatial and temporal pattern of soil thaw was modelled on a 25 535 m² area of interest (AOI) on a north-facing alpine tundra hillslope in southern Yukon, Canada. Daily oblique photographs were used to pixilate the AOI and measure the snow cover depletion for the AOI. Transects of thaw depth through selected snow-free patches within or adjacent to the AOI were used to provide spatial representation of thaw depth and saturated hydraulic conductivity. To compute thaw depth for each pixel within the AOI as it became snow-free, a finite element geothermal model was driven from meteorological forcing and soil hydro-thermal data. Daily maps of snow-free area and thaw depth were generated for the AOI, which were then combined with information on flowpath tortuosity and depth-integrated saturated hydraulic conductivity for snow-free areas to provide a drainage rate for the AOI. This drainage rate varied with the spatial arrangement of the snowpack and soil thaw depth. At the beginning of melt, the lack of hydrological connectivity for the AOI inhibited drainage. The drainage rate was maximized during the mid-melt period since sub-surface connections among snow-free patches were widespread, and the hydraulic conductivity of the sub-surface flow zone was still relatively high, owing to shallow soil thaw depths. Drainage was low at the end of the melt period because the frost table was at a depth where the hydraulic conductivity was very low. The results of this study indicate that to accurately simulate runoff at the hillslope scale during snowmelt, both the spatial pattern of snowmelt and ground thaw should be considered. Copyright © 2009 John Wiley & Sons, Ltd.

KEY WORDS permafrost; snowmelt; active layer thaw; sub-surface runoff; modelling

Received 7 July 2008; Accepted 16 March 2009

INTRODUCTION AND BACKGROUND

Tundra is a treeless terrain with a continuous organic cover underlain by permafrost, and is ubiquitous in much of northern Canada and the circumpolar arctic (National Research Council of Canada, 1988). In exposed and topographically complex alpine environments, wind redistributes snow during the long accumulation period from areas of high exposure to sheltered sites, resulting in large variations in snow water equivalent prior to melt (Pomeroy *et al.*, 1993). Large, deep snow drifts on leeward slopes often persist on the landscape for 4 or more weeks following the melt of the surrounding snow cover. The timing and magnitude of runoff from an alpine tundra hillslope depend strongly on its aspect that influences the surface energy balance and snow water equivalent (e.g. Lewkowicz and French, 1982; Carey and Woo, 1998; Pomeroy *et al.*, 2003). For example, north-facing slopes have relatively small snowmelt and ground

thaw rates, resulting in prolonged snowmelt periods and relatively large runoff ratios (Slaughter and Kane, 1979; Carey and Woo, 1998). Runoff from north-facing exposures is enhanced in cases where these exposures are also leeward slopes that accumulate deep snow covers. The contrast in runoff production from hillslopes of different aspect is especially pronounced in the zone of discontinuous permafrost, where north-facing aspects (in the northern hemisphere) support permafrost due to a lower surface net energy balance, whereas opposing slopes do not. For example, Carey and Woo (1998) reported that south-facing slopes in Wolf Creek, southern Yukon, are permafrost-free and are therefore able to dampen runoff production by routing a relatively high proportion of meltwater input into sub-surface storage and deep percolation.

Hillslope runoff simulations have been conducted in a variety of alpine and permafrost environments, with runoff related to various spatially distributed slope factors, including near-surface saturated hydraulic conductivity (Orlandini *et al.*, 1999), the topographic index $\ln A/\tan\beta$ (Stieglitz *et al.*, 2003; Wetzel, 2003), frozen

* Correspondence to: William L. Quinton, Cold Regions Research Centre, Wilfrid Laurier University, Waterloo, N2L 3C5, Canada.
E-mail: wquinton@wlu.ca

ground (Quinton *et al.*, 2004; Bayard *et al.*, 2005) and snow cover (Swamy and Brivio, 1997; Schaper *et al.*, 1999; Kolberg and Gottschalk, 2006). However, several diagnostic features of slopes in alpine tundra are not well represented in runoff models. For example, tundra conveys little or no flow on its surface due to the large water-holding capacity of organic soils (Slaughter and Kane, 1979; Carey and Woo, 2001) and their high-frozen and unfrozen infiltration rates (Hinzman *et al.*, 1993) that far exceed the rate of input from snowmelt or rainfall. Snow drifts play an important role in hillslope runoff through (i) concentrating runoff to areas downslope of their position (Lewkowicz and French, 1982) and (ii) controlling the daily pulse of meltwater percolate to the ground surface below the drift (Quinton and Pomeroy, 2006). The subsequent lag between the release of meltwater from the bottom of snow drifts and its arrival at the stream depends on the properties of the intervening hillslope, including its angle and length (Dunne *et al.*, 1976; Rydén, 1977). Recent studies have demonstrated that the degree of ground thaw on the snow-free tundra downslope of the drift also strongly influences the rate at which the daily meltwater wave is conducted across it to the streambank (e.g. Carey and Quinton, 2005).

The ground begins to thaw once it has become snow-free. Ground thaw continues if sufficient energy is supplied, as indexed by air temperatures remaining more than 0°C. Since the ground below the frost table is typically saturated with ice and a small amount of unfrozen water, the frost table acts as a semi-impermeable aquitard and represents the lower boundary of the sub-surface flow zone—the thawed portion of the saturated soil that conducts runoff. The horizontal, saturated hydraulic conductivity (K_s) of peat decreases by several orders of magnitude with depth over the upper 0.5 m of organic soil in cold regions (e.g. Quinton and Marsh, 1998; Carey and Woo, 2001). Quinton *et al.* (2008) examined the K_s profiles of several widely occurring types of organic-covered permafrost terrain and found that all exhibited a uniformly high and low K_s in the upper and lower regions of the profile, respectively, separated by a transition zone in which K_s decreases abruptly with depth (Figure 1). The authors proposed K_s as a continuous function of depth below the ground surface z [L]:

$$\log K_s(z) = \frac{\log K_{s(\text{btm})} + (\log K_{s(\text{top})} - \log K_{s(\text{btm})})}{\left[1 + \left(\frac{z}{z_{\text{trn}}}\right)^n\right]} \quad (1)$$

where $K_{s(\text{top})}$ and $K_{s(\text{btm})}$ are the saturated hydraulic conductivities (L T^{-1}) of the top and the bottom of the peat profile, z_{trn} [L] is the transition depth, and n is a dimensionless constant governing the shape of the transition curve. The mean K_s of the sub-surface flow zone (K_f) is an intermediate value between the hydraulic conductivities of the top (i.e. water table) and bottom (i.e. on the frost table surface) of the sub-surface flow zone (Figure 1). The water table depth is highly variable

over space and time, and as a result, errors resulting from using estimated water table depths to derive K_f would be large. An alternate method of deriving K_f is to assume equivalence between it and the hydraulic conductivity at the bottom of the sub-surface flow zone (K_{FT}). Although the $K_f \sim K_{\text{FT}}$ assumption underestimates the value of K_f , the difference is assumed to be small since the sub-surface flow zone is typically thin on the study slope compared with valley bottom areas, given the relatively large topographic gradient of the former.

The influence of the degree of ground thaw on K_f illustrates the close coupling of the water and energy fluxes in tundra environments. The cumulative ground heat flux during the thaw season for organic-covered permafrost terrains, where conduction is the primary thermal transfer mechanism, is typically ~20% of cumulative net radiation (Halliwell and Rouse, 1987; Carey and Woo, 2000). The large majority (>80%) of the ground heat flux is used to melt ice in the active layer (Hayashi *et al.*, 2007). An earlier study on the same hillslope demonstrated that little or no ice is present above the frost table during soil thawing, and that the latent heat flux below the ground is predominantly used to lower the frost table (Quinton *et al.*, 2005). Temporal variations of K_f have been derived from measured (Wright *et al.*, 2008) and computed (Hayashi *et al.*, 2007) soil thaw for discrete points on hillslopes. However, if the spatial distribution of the frost table depth on hillslopes is known, the depth dependency of the K_s (Figure 1) can be used to estimate the spatial distribution of K_f and spatially integrated values of the latter for hillslopes.

In recent years, high-quality remote sensing data at different resolutions have become increasingly available, making it possible to map snow cover disappearance at reasonably frequent time intervals for various spatial scales (e.g. Salomonson and Appel, 2004; Beck *et al.*, 2005; Nagler *et al.*, 2008). Mathematical methods to simulate active layer thaw (e.g. Goodrich, 1978, 1982a, b; Riseborough, 2004; Woo *et al.*, 2004; Hayashi *et al.*, 2007; Zhang *et al.*, 2008) provide efficient tools to map ground thaw from climate data and the spatial distribution of snow cover. Furthermore, by simulating thaw spatially at the hillslope scale, information unobtainable at the point and plot scales, such as the spatial and temporal patterns of K_f , tortuosity of flow pathways and slope-integrated drainage rates can be obtained. Considering this, the objective of this study is to examine the efficacy of obtaining reasonable estimates of spatially representative drainage parameters for an alpine tundra hillslope during snowmelt from relatively simple computations and limited field measurements.

STUDY SITE

The study was conducted at Granger Basin (60°32' N, 135°18' W), a sub-catchment of the Wolf Creek Research Basin, 15 km south of Whitehorse, Yukon Territory, Canada, during 2002 and 2003 (Figure 2). The

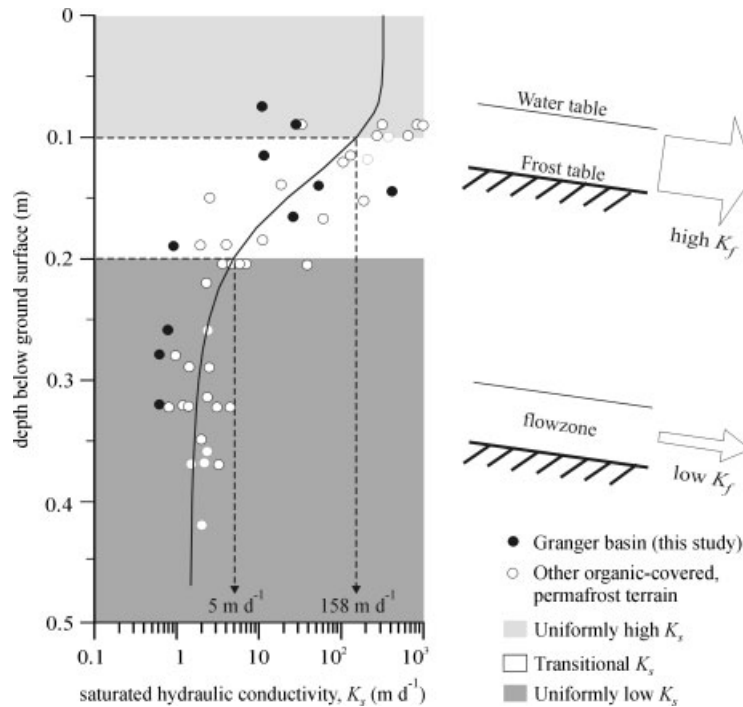


Figure 1. Depth variation of saturated horizontal hydraulic conductivity measured from tracer (KCl^-) tests conducted at the site of the present study, as well as at other organic-covered permafrost terrains in north-western Canada, as reported by Quinton *et al.* (2008). The curve through the data is defined by Equation (1). The light and dark grey indicate the zones in which K_s is uniformly high and uniformly low, respectively. The schematic indicates the decrease in the mean hydraulic conductivity of the saturated flowzone (K_f) with active layer thaw. Modified from Quinton *et al.* (2008)

area has a subarctic continental climate characterized by a large temperature range and low precipitation. Mean annual January and July temperatures from the Whitehorse airport (elevation 706 m a.s.l.) are $-17.7^\circ C$ and $+14.1^\circ C$, respectively. Mean annual precipitation is 267 mm, of which, 122 mm falls as snow (1971–2000). Granger Basin drains an $\sim 8 \text{ km}^2$ area and ranges in elevation from 1310 to 2250 m a.s.l. The main river valley trends west to east at lower elevations, resulting in hillslope aspects that are predominantly north and south facing. Permafrost occurs at higher elevations and on north-facing slopes (Lewkowicz and Ednie, 2004).

Granger Basin supports a near-continuous organic cover of sphagnum moss, supporting various herbs, including Labrador tea (*Ledum* sp.), sedges, grasses and lichens. The thickness of the organic soil decreases with distance upslope from $\sim 0.4 \text{ m}$ in the valley bottom to $\sim 0.08 \text{ m}$ near the crests. The upper $\sim 0.1\text{--}0.15 \text{ m}$ zone is composed of living and lightly decomposed vegetation, overlying a more decomposed layer.

The study was conducted near the outlet of Granger Creek on a 17.5° north-facing slope underlain by a 15 to 20 m thick permafrost layer (Pomeroy *et al.*, 2003). The length of the slope from its crest to the streambank is approximately 150 m. Each year, a snow drift forms on the upper part of the slope (Figure 2) and persists for 4 to 5 weeks after the disappearance of the surrounding snow cover. The drift has a maximum snow depth in the range of 2–3 m, extends $\sim 350 \text{ m}$ across the slope and $\sim 40 \text{ m}$ in the slopewise direction.

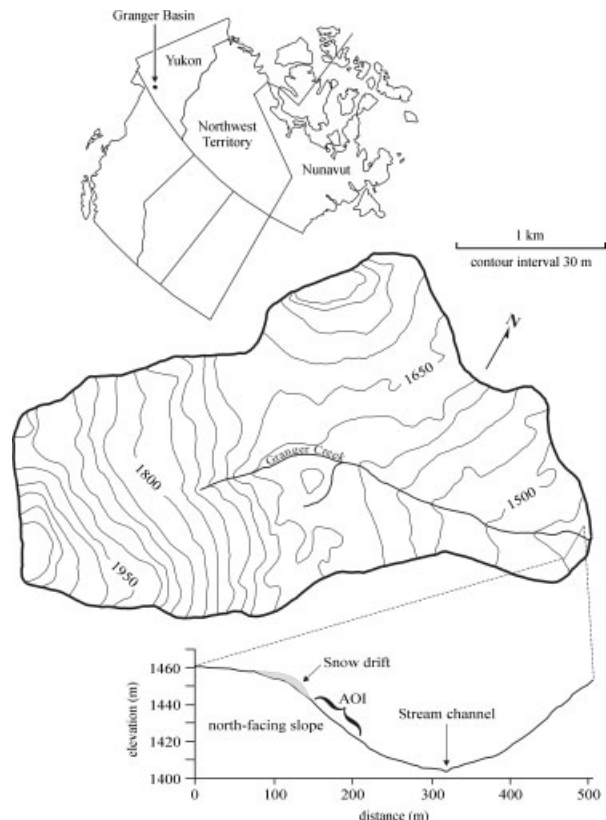


Figure 2. The area of interest in Granger basin located downslope of a late-lying drift on the north-facing slope

Overland flow was not observed anywhere on the hill-slope during the study, and hillslope runoff was therefore conveyed through the active layer, the maximum

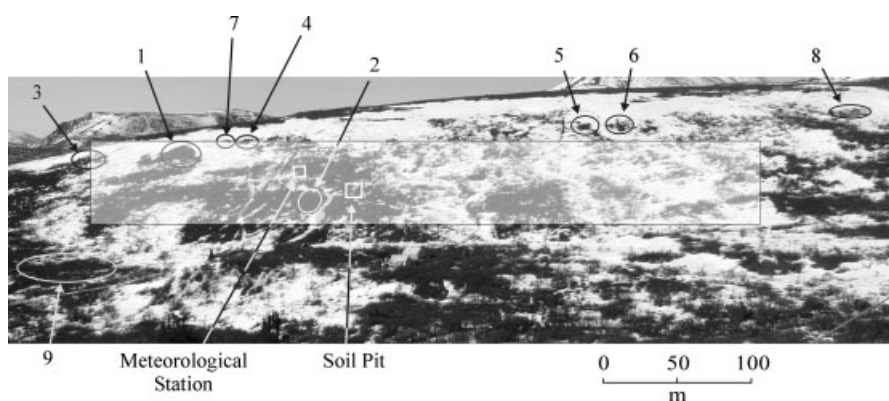


Figure 3. Photograph of the north-facing slope taken from the opposite slope on 1 May, 2003, showing the locations of the nine snow-free patches, the instrumented pit and the meteorological tower. The area of interest (AOI) is indicated by the rectangle. On the photograph, the lower edge of the AOI is the downslope edge

thickness of which ranged between ~ 0.4 m on the slope crest and >1 m near the slope base. At the time the ground surface became snow-free on the study slope, the relatively impermeable frost table was typically within the upper 0–0.05 m depth range. It then descended through the soil profile as the active layer thawed.

METHODOLOGY

Daily measurements of frost table depth were made using a graduated steel rod at 0.5 m intervals along a transect line within nine snow-free patches on the hillslope (Figure 3). The transects were oriented parallel to the slope, and as the snow-free area progressively increased, each transect was lengthened to include new measurement points at 0.5 m increments. Eventually, the nine transects contained between 12 and 39 points. Digital photographs of the north-facing study slope were taken daily from the opposite slope to document the growth of the snow-free patches during the melt period. The resolution of the images corresponded to a nominal pixel size of $0.28 \text{ m} \times 0.28 \text{ m}$. A $25\,535 \text{ m}^2$ ($436.5 \text{ m} \times 58.5 \text{ m}$) area of interest (AOI) on the north-facing slope was treated as an observation and modelling control unit for processes operating at the hillslope scale, while point/transect and plot scale observations were made simultaneously within the AOI. Image-to-image registration was performed to align the daily photographs. This was followed by a *k*-means clustering of the data (Arkin and Colton, 1956; Mendenhall *et al.*, 1999) to classify snow cover for each image. From the daily photographs, binary images were generated that distinguished snow-covered from snow-free pixels within the AOI. It was assumed that soil thaw at a pixel began once it became snow-free; therefore, the images provided the starting date of soil thaw for each pixel and the spatial pattern of snow disappearance and soil thaw initiation within the AOI.

A soil pit was excavated to the permafrost table in August, 2001 at a point near the centre of the AOI (Figure 3). The upper 0.15 m was composed of living and lightly decomposed fibric peat overlying a lower

0.19 m thick layer of sylvic peat containing dark woody material and the remains of mosses, lichen and rootlets. The lowest 0.06 m was mineral sediment. Volumetric soil moisture sensors (Campbell CS615, accuracy $\pm 3\%$) were installed into the pit face at 0.02, 0.05, 0.10, 0.20, 0.30 and 0.40 m below the ground surface, and soil temperature sensors (Campbell 107B, accuracy $\pm 0.2^\circ\text{C}$) were installed into the pit face at 0.02, 0.05, 0.075, 0.10, 0.15, 0.20, 0.25, 0.30, 0.35 and 0.40 m below the ground surface. This single pit was assumed to represent the average ground thermal properties of the AOI owing to the very low variation in slope angle (5° of the mean of 20°), sky view, surface albedo and organic soil thickness (Pomeroy *et al.*, 2003). Air temperature was measured with a Vaisala HMP45C temperature and relative humidity sensor placed 2 m above the ground surface at a meteorological station located 10 m upslope of the soil pit (Figure 3). Measurements were made every minute and averaged and recorded on a Campbell Scientific CR10X datalogger every half hour.

Simulation of ground thaw

Figure 4 describes the simulation of ground thawing depths after snowmelt by a one-dimensional thermal conduction model (TONE; Goodrich, 1978, 1982a, b; Riseborough, 2004). TONE uses a finite element numerical scheme and the thawing/freezing latent heat was parameterized as an apparent heat capacity. The model ran on 30-min time steps, and was implemented in 15 soil layers to a depth of 5 m. The spacing of nodes increased progressively with depth, and was between 0.05 and 0.1 m in the top 0.7 m. The fine time and soil layer resolutions chosen in this study were to ensure the smooth convergence of the numerical model. The 5 m soil column was to satisfy the assumed lower-boundary condition of zero heat flux (Zhang *et al.*, 2008). The model was driven by the ground surface temperature derived from the measured air temperature and a ratio of ground surface and air temperatures, defined as the N-factor in geothermal studies (e.g. Klene *et al.*, 2001). In this study, a site-calibrated constant N-factor is used

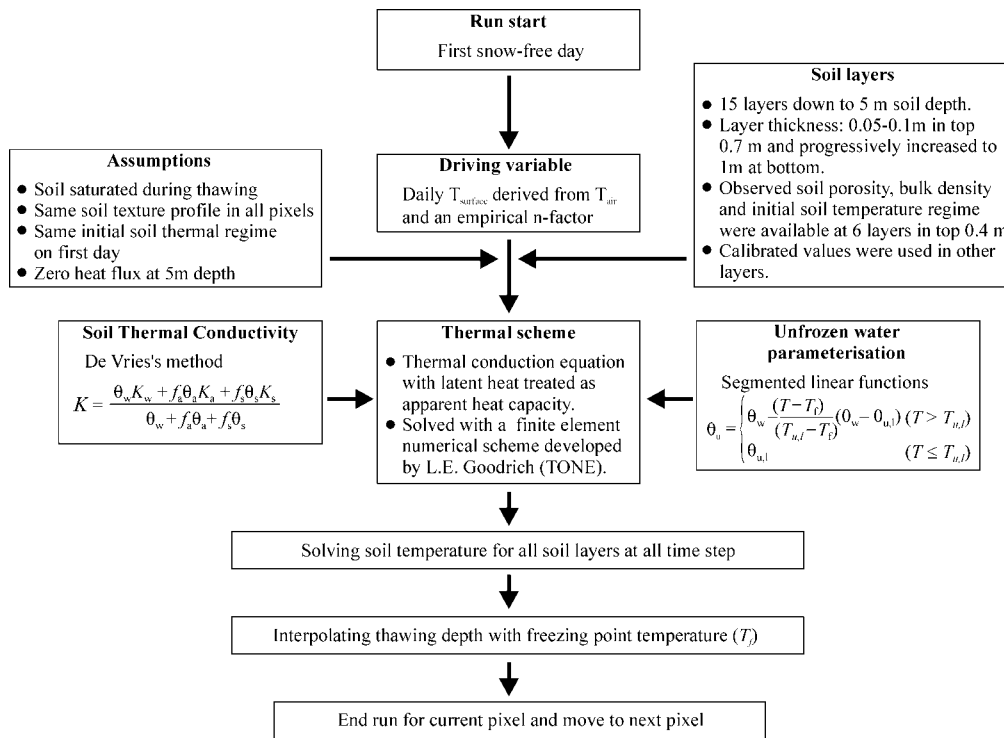


Figure 4. Schematic description of the method to derive daily series of active layer thaw maps

due to the small variations of surface and soil conditions within the AOI.

The related study by Quinton *et al.* (2005) demonstrated that for the period 17 May to 8 July 2003, the cumulative ground heat flux at the soil pit was 20% of the cumulative net all-wave radiation. Because this proportion was also reported by Halliwell and Rouse (1987) and Carey and Woo (2000) for organic-covered permafrost where conduction is the dominant thermal transfer process, it is suggested that advection of energy to the soil pit is not a major contributor to soil thaw. Conduction appears to be the dominant thermal transfer process at the nine snow-free patches as well, given the rates of thaw at each patch relative to the cumulative net all-wave radiation (Quinton *et al.*, 2005, p. 380, Figure 7).

A three-step scheme (Figure 5) was implemented to produce a time series of daily thaw depth maps based on the snow cover depletion within the AOI. The calibration of the TONE model in simulating ground thaw was conducted near the soil pit using detailed observations of soil physical properties, soil temperature and moisture and air temperature data from the meteorological station. Soil temperatures at 0.02 m depth were used to drive the model. A carefully designed procedure as described in Zhang *et al.* (2008) was followed to select the most appropriate methods of thermal conductivity and unfrozen water parameterization methods as well as the site-specific parameters by comparing the simulated thawing depth with the data derived from the detailed soil temperature measurements. The same calibration method was used to quantify the initial soil temperature and moisture conditions below 0.4 m soil depth. Once the above

calibration goals were achieved, ground surface temperature values, obtained by applying an assumed N-factor to the air temperature, were used to drive the model. The site-specific N-factor was found by trial and error to optimise the thaw depth simulations. Those parameters and initial values were adopted in the following validation and application processes.

Validation of TONE was conducted on five (1, 2, 5, 6 and 7) of the nine patches with good-quality snow depletion images and observed organic layer depths. Minimum bounding rectangles (e.g. Figure 6) were defined for all five test patches based on their snow-free area and transect length on the final day of frost table depth measurement (3 June 2003 for patches 1, 2, 6 and 7; and 4 June 2003 for patch 5). The simulated thaw depths of all pixels within each rectangle were averaged each day at the times coinciding with the transect measurements. For each patch, the daily average simulated thaw depth was plotted with the average measured value (Figure 7). To compare the patch and transect representative values of frost table depth, all pixels and transect points that were snow-free by 4 June were included in the calculation of the average simulated and measured values for all preceding days. The thaw depth of pixels and transect points was assigned a value of zero until they became snow-free.

On satisfactory model performance, thaw simulations for each of the 1259 × 209 pixels within the AOI were made and daily active layer thaw maps generated for the period from 24 April, when the snow cover fell below 100% of the AOI, to 12 June, 5 days after the entire AOI became snow-free. A map of first snow-free date of the AOI was used to activate the thaw depth simulation

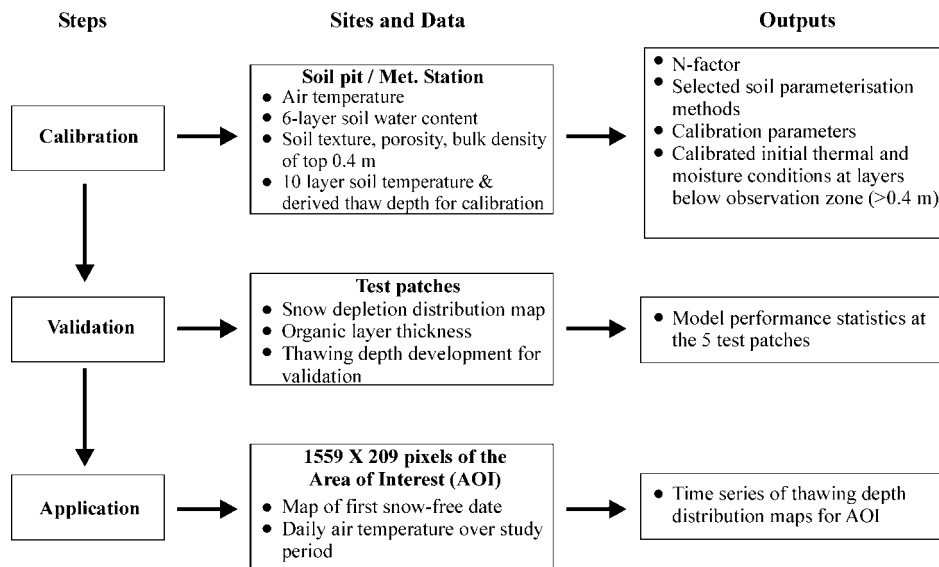


Figure 5. Schematic description of the model calibration, validation and application of TONE

when the pixel became snow-free. The air temperature observed at the meteorological tower and the calibrated N-factor were used to drive the model.

The influence of snow cover distribution on drainage

Previous studies on the north-facing slope at Granger Basin (Quinton *et al.*, 2004, 2005) demonstrated that snow patches largely obstruct hillslope drainage from flowing below or through them and deflect water into their surrounding snow-free areas. This is due to the relatively impermeable frost table below snow patches remaining at or very close to the ground surface until the snow disappears. In this study, snow-covered pixels were therefore assumed to represent relatively non-conductive portions of the AOI. To quantify the importance of tortuosity of sub-surface flow through the AOI resulting from snow cover, the particle-tracking technique of Quinton and Marsh (1998) was applied to each daily image of the AOI. Each image was first converted to binary, where pixels with a value of 0 were snow-covered, and those with a value of 1 were snow-free and therefore able to conduct sub-surface drainage.

Water particles were moved pixel by pixel downslope through the AOI. For each date between 25 April and 14 June, 39 particle runs were performed, one each at 39 equally spaced pixels along the first row of each image. If the first pixel was snow-covered, then the path was terminated, otherwise the particle moved downslope until a snow pixel was encountered, and a lateral flow direction was determined by the generation of a random number between 0 and 1. If the value was >0.5, a left turn was made; otherwise, the particle turned right. If both the right and left pixels were snow-covered, the run was terminated. Lateral flow continued until a snow-free pixel on the downslope side was encountered, allowing downslope movement, or a snow-covered pixel was encountered, causing the run to terminate. It was not deemed necessary to allow water that cannot move

laterally to accumulate and back-up so that it could then flow along a row of pixels higher on the hillslope, since no ponding of water was observed in the field on the upper edge of snow patches.

Tortuosity, T_x , was computed for each run terminating at the downslope edge of the AOI from:

$$T_x = \frac{L_f}{L_s} \tag{2}$$

where L_f is the flow distance measured by the number of pixels encountered by a particle between the beginning and end of the run at the bottom row of pixels in the AOI, and L_s is the straight-line distance between the upper and lower edges of the AOI, equal to 209—the number of pixel rows in the AOI. Average T_x values for the entire AOI ($T_{x(AOI)}$) were computed for each day from 1 April to 7 June.

To calculate a spatially representative K_f on the entire AOI, probability frequency distributions (PFD) of thaw depth were computed for each day at a 0.01 m interval using the TONE-simulated daily thaw maps to a maximum thaw depth. The depth-dependent PFD values ($P(z)$) were then used to derive a spatial representative K_f ($K_{f(AOI)}$) by

$$K_{f(AOI)} = \int P(z)K_f(z) = \sum_{i=0}^N P_i K_{f,i}, \tag{3}$$

where $K_f(z)$, or its discrete form $K_{f,i}$, could be quantified by Equation (1). P_i is the PFD value of each thaw depth interval (i) for all the intervals (N). Where the frost table is at the ground surface, $i = 0$, in which case the active layer is non-conductive (i.e. does not contain a sub-surface flow zone), and $K_{f,i}$ was assigned a value of 0.

To illustrate the application of this spatially representative hydraulic conductivity for sub-surface flow, the mean transit time (t_{AOI}) of sub-surface flow across the

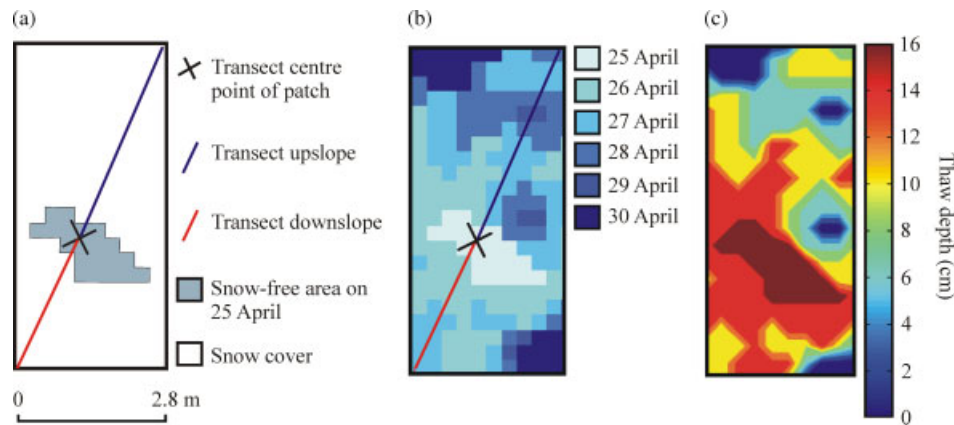


Figure 6. (a) An 18.5 m² minimum bounding rectangle containing the snow-free area that defined patch 2 on 25 April, 2003, with the upslope and downslope portions of the frost table-depth measurement transect, relative to the initial measurement point in the middle of the patch. (b) The growth of the snow-free patch 2 from 25 to 30 April. (c) The frost table depth within the minimum bounding rectangle on 1 May, 2003

entire AOI for each date was computed by the following equation:

$$t_{\text{AOI}} = \frac{L_s T_{x(\text{AOI})}}{[K_{f(\text{AOI})} \sin(\alpha)]} \quad (4)$$

where $\sin(\alpha)$ accounts for the slope (α) effect on the sub-surface flow and represents the hydraulic gradient (flow driven by topographic gradient). When $\alpha = 0^\circ$, the AOI terrain is flat and no sub-surface flow is generated as t_{AOI} becomes infinite. When $\alpha = 90^\circ$, flow is vertical and at its maximum rate (equal to the hydraulic conductivity) and the transit time would be at a minimum.

RESULTS AND DISCUSSION

Most of the model calibration results for this site were presented in Zhang *et al.* (2008) and will not be repeated here. A segmented linear function was used to parameterise the unfrozen water content, and soil thermal conductivity was parameterised using the de Vries method (Figure 4) that proved superior after comparing with other parameterization schemes. The calibrated parameters for each soil layer can be found in Zhang *et al.* (2008). When driven by observed 0.02 m soil temperature and calibrated parameters and initial values, the root mean square differences (RMSD) between the simulated and observed thaw depth was 0.02 m. When driven by air temperature and the calibrated N-factor, the RMSD increased to 0.05 m. The calibrated N-factor for this site is 0.85, which is comparable with the values reported for a similar site condition in Alaska by Klene *et al.* (2001).

Figure 6 uses patch 2 as an example of how TONE was validated. The growth of patch 2 from its initial size on 25 April (Figure 6a) and the pattern of snow-cover removal during the following 5 days (Figure 6b) are shown within an 18.5 m² minimum bounding rectangle around the snow-free area of 30 April. The original snow-free patch area of 25 May is shown as the area of deepest thaw in the TONE-simulated spatial distribution of frost table depth for 1 May (Figure 6c). Considering the depth variation of K_s (Figure 1), the 0–16 m thaw depth range shown in

Figure 6c implies that K_f varies by one or two orders of magnitude within the 18.5 m² area of patch 2. Figure 6c also indicates that the pattern of ground thaw and the frost table depth statistics derived from transect measurements could vary substantially if the orientation of the transect line was changed.

For each patch, the daily average simulated thaw depth was plotted with the average measured value (Figure 7). The TONE simulation showed reasonable agreement with average measured frost table depth at all five test patches. Prior to 16 May, re-freezing events and snowfall caused greater fluctuations in the simulations than were observed (Figure 7). In the case of patch 2, TONE reset the frost table to the ground surface in response to re-freezing in the 12–14 May period, and as a result, TONE underestimated actual thaw by ~ 0.1 m by the end of the simulation on 4 June. At the other four test patches, TONE produced final thaw depths all within ~ 0.08 m of the measured values, three of which overestimated measured thaw. Because soil thaw on any day is the sum of the daily total thaw and freeze-back since the initial snow-free day, the final simulated thaw values presented in Figure 7 include the sum of errors throughout the simulation. However, since Figure 1 indicates that K_s is uniformly high in the upper ~ 0.1 m of soil, and uniformly low at depths greater than ~ 0.2 m, the consequence of errors in simulated thaw depth on the predicted value of K_f is minimal when the frost table is above or below the 0.1–0.2 m depth range.

With satisfactory results from the validation of TONE on the five test patches, TONE was then applied to compute cumulative thaw for all pixels within the entire AOI as they became snow-free. Although the cumulative thaw depth was computed for each day, four dates with contrasting snow-covered area percentages are presented: 25 April (95%), 30 April (70%), 19 May (25%) and 7 June (0%). As air temperature (Figure 8) was well above freezing on 24 April, some pixels covered by shallow snow became snow-free. Two periods (1–6 May and 12–16 May) with below freezing air temperatures

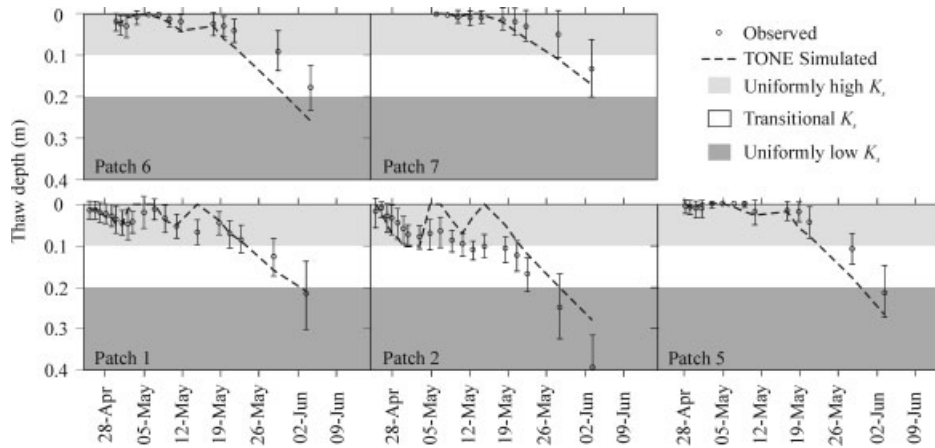


Figure 7. TONE-model validation results using observed thaw depths from the five test patches. The light and dark grey indicate the zones in which K_s is uniformly high and uniformly low, respectively. The error bars indicate one standard deviation above and below the mean

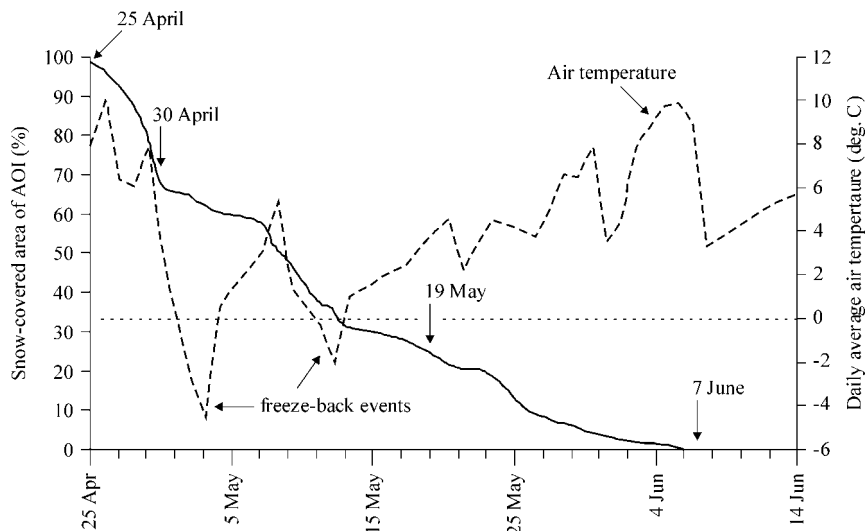


Figure 8. The mean daily air temperature and depletion of the snow-covered area within the area of interest (AOI). The left vertical axis also indicates the complimentary increase in the percentage of the AOI that is snow-free and therefore contains a sub-surface flowzone, defined by the presence of a water table and frost table below the ground surface, as illustrated in Figure 1

occurred early in the snowmelt period, halting snowmelt and causing the ground to re-freeze.

The spatial pattern of snow-cover removal (Figure 9a) is closely followed by that of soil thaw (Figure 9b). The >95% snow-cover on 25 April suggests that the sub-surface flow zone was present on only ~5% of the AOI (Figure 8). Figure 9 indicates that this small percentage is distributed widely throughout the AOI, and as a result, sub-surface water conveyance to the valley bottom was ineffectual at that time, despite the high K_f (>346 m day⁻¹) of the thawed (i.e. snow-free) portions of the AOI. By 30 April, the snow-covered area had diminished to 75% of the AOI, allowing much of the previously isolated snow-free area to coalesce into a tortuous, but continuous, sub-surface flowzone connecting the upslope and downslope edges. With the frost table depth within the upper 0.15 m of soil, K_f values were high or transitional throughout the AOI. The re-freezing period of 12–16 May, during which daily average air temperatures ranged between -2.3 and -0.2 °C, resulted in a thawing depth drawback that was

still evident by 19 May (Figure 9b). The high degree of hydrological connection among snow-free areas, and the large K_f (>346 m day⁻¹) of those areas, made the AOI a highly efficient sub-surface flow conveyor by 19 May. It was also in this period that the late-lying snow drift was actively melting and supplying daily meltwater pulses to the upslope edge of the AOI. By 7 June, the sub-surface flowzone occupied the entire AOI, and therefore, the tortuosity of flow resulting from areas of unthawed (i.e. snow-covered) ground would have been at a minimum. However, with the exception of a few hydrologically isolated areas with transitional flow values, K_f was mostly in the lower range throughout the AOI.

A general pattern of increasing thaw depth with time throughout the AOI is observed when comparing the PFDs presented in Figure 10. However, this pattern is interrupted by the freeze-back events identified in Figure 8, as reflected in the PFD curve of 19 May. The critical factor regarding the effect of snow cover on flow is whether or not snow-free pathways to the valley bottom

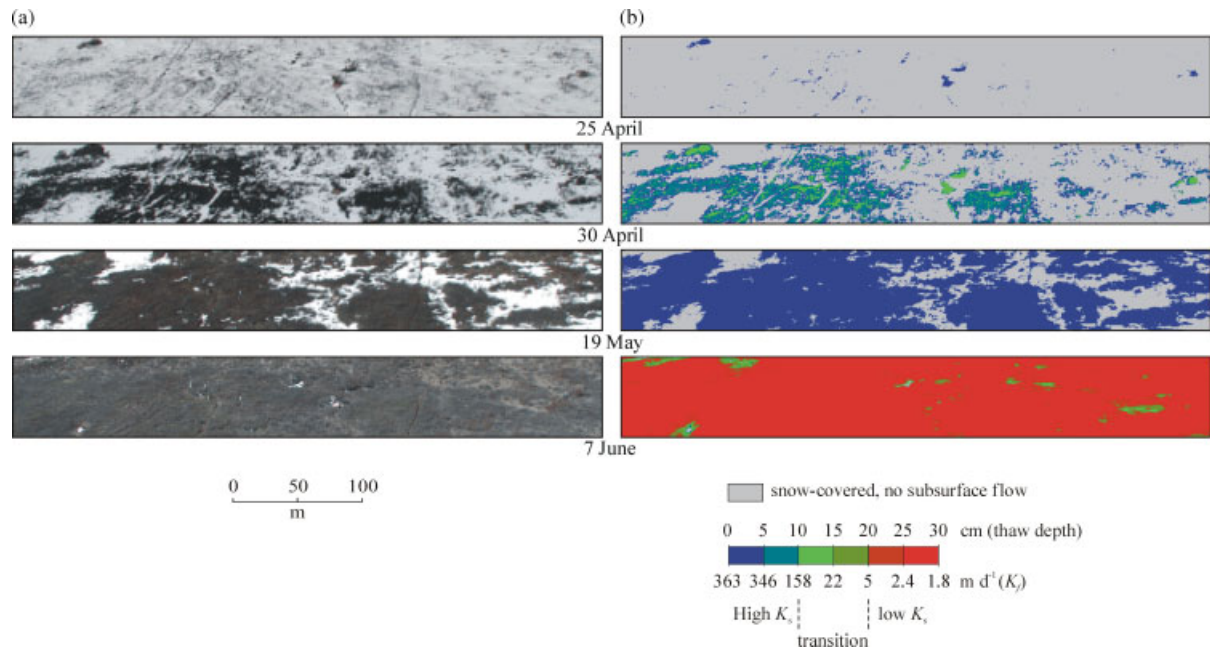


Figure 9. The snow cover (a) and TONE-simulated frost table depth (b) within the area of interest (AOI) on 25 and 30 April, 19 May and 7 June, 2003. The spatial distribution of the hydraulic conductivity corresponding to the frost table depth (K_{FT}) was estimated for each snow-free pixel in the AOI from Equation (1). Figure 9b also serves as a plot of the spatial distribution of K_f , assuming $K_f \sim K_{FT}$

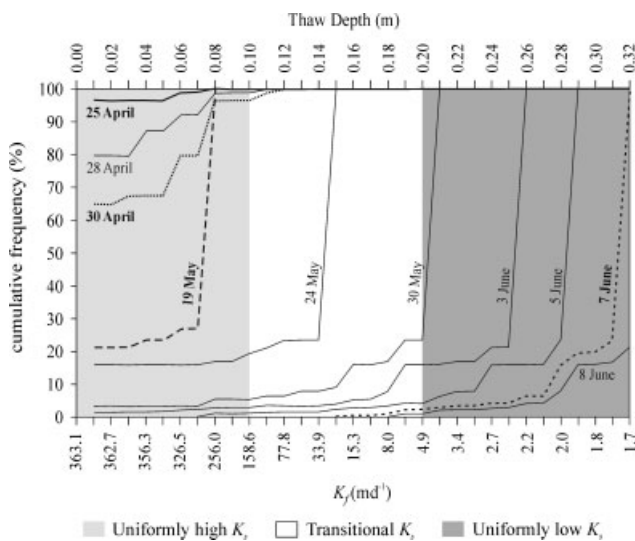


Figure 10. Cumulative probability frequency distributions (PFD) of TONE-simulated thaw within the area of interest. The four sample dates presented in Figures 8 and 9 are identified in bold text and heavy lines. The PFD curves of six additional dates are also included to more completely demonstrate the temporal variation in PFD. The light and dark grey indicate the zones in which K_s is uniformly high and uniformly low, respectively

exist. For example, such pathways were absent in the AOI on 25 April (Figure 9a), and therefore the snow cover would have obstructed flow, even though the K_f distribution for that date in Figure 10 implies a very high rate of localized sub-surface flow.

Figure 11 illustrates the evolution of the spatially averaged tortuosity and hydraulic conductivity of the AOI during the study period. Since the growth and aggregation of snow-free patches increased the connectivity of the sub-surface flow zone, the average daily tortuosity

exhibited a general decreasing trend during the thawing period, although some slight increases occurred during the two freeze-back periods. $T_{x(AOI)}$ decreased from 3.7 to 1.2 between 1 and 20 May, and then to the lower limit of 1.0 by 7 June. However $K_{f(AOI)}$ varied more than two orders of magnitude during the same period. Lower $K_{f(AOI)}$ values occurred in the early snowmelt period and then again late in that period: the former caused by the zero-flow condition of snow-covered pixels and the latter by the low K_f resulting from the greater thaw depth and therefore greater depth of the sub-surface flow zone. The high $K_{f(AOI)}$ value during the middle of the snowmelt period coincided with the widespread development and aggregation snow-free patches and high K_f values resulting from the shallow depth of thaw. The effect of tortuosity on the transit times through the AOI is small compared with K_f during the same period as demonstrated by the transit time evolution in Figure 12. The t_{AOI} variation was predominantly inversely related to the development of $K_{f(AOI)}$. Figure 12 also indicates that during the early and late snowmelt period, sub-surface flow is strongly inhibited within the AOI.

Although this analysis has largely focussed on spatially averaged properties of the AOI, the field observations and model simulations have also provided valuable insight into localized (i.e. within-AOI) thaw and flow behaviour. As a result, a conceptual model has begun to emerge that relates local variations in thaw depth and sub-surface drainage patterns. Areas of increased soil thaw are manifested as depressions in the frost table topography that consequently collect drainage from surrounding areas. For example, Figure 6c indicates that on 1 May, the frost table depression near the centre of the image was approximately 0.15 m deeper than

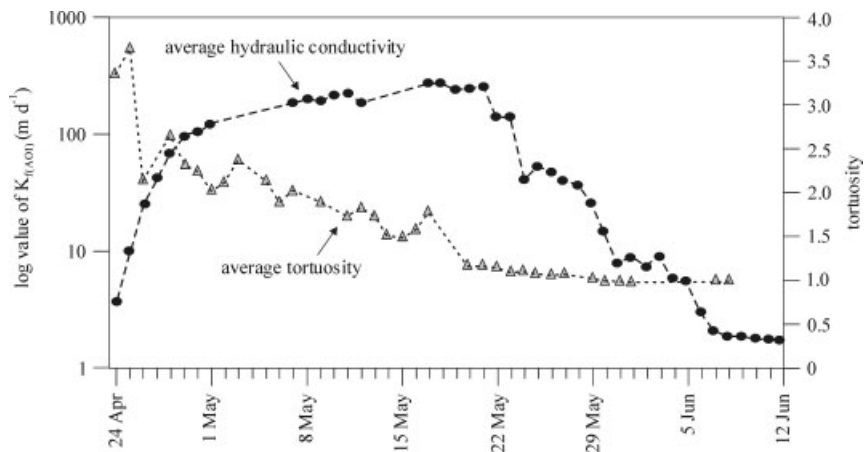


Figure 11. Daily development of area of interest (AOI) averaged hydraulic conductivity of sub-surface flow derived from the daily thaw maps, and the average daily tortuosity of sub-surface drainage pathways within the AOI, resulting from the presence of snow patches

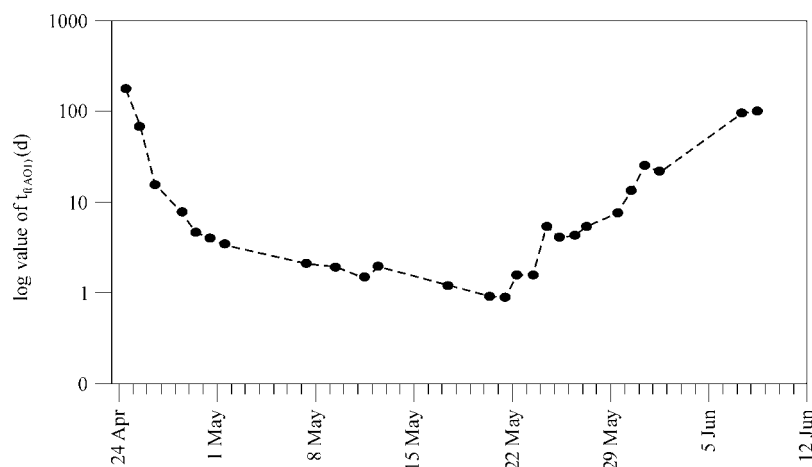


Figure 12. Daily development of area of interest (AOI) averaged transit time of sub-surface flow through the AOI estimated by Equation (4)

points <1 m away. Frost table depressions therefore become areas of increased soil moisture and saturated layer thickness, and since wetter soil is a better conductor of energy from the ground surface to the frost table (Hayashi *et al.*, 2007), they also receive additional energy from the ground surface, leading to further soil thaw. With regard to soil storage, frost table depressions are more effective at retaining water given the much lower horizontal hydraulic conductivity at depth. As long as the water table elevation of such areas is lower than that of surrounding areas, frost table depressions continue to collect local drainage and, unless internally drained, can also provide a preferential pathway for sub-surface drainage from the hillslope.

SUMMARY AND CONCLUSIONS

This study demonstrated that the spatial pattern of snow cover removal on an organic-covered hillslope with permafrost governs the spatial pattern of soil thaw since thaw commences once the ground becomes snow-free. It was also shown that the soil thaw rate on such hillslopes can be accurately simulated from the areal depletion of the snow cover. A K_s -depth association developed

specifically for organic-covered permafrost terrains was used to simulate the spatial distribution of the hydraulic conductivity of the sub-surface flow zone K_f on a daily time step on a >25 000 m² hillslope area as it became snow-free. The nature of the K_s -depth association is such that the effect of variations of soil thaw on flow is minimal when the frost table is above or below the 0.1–0.2 m depth range throughout the hillslope.

This study emphasized the importance of hillslope-scale patterns of snowmelt and soil thaw on sub-surface drainage. Point or plot scale observations would neglect the important spatial effect that both melt and ground thaw has on drainage, leading to an overestimation of drainage in the early stages of snowmelt when the sub-surface flow zone is widely obstructed by the snow cover, and when continuous flowpaths to the valley bottom are few in number and highly tortuous. As snowmelt progressed and snow-free patches expanded and coalesced, flowpath tortuosity reduced, as did the non-conductive (i.e. snow-covered) portion of the hillslope, while the minimum K_f in the snow-free areas decreased by one to two orders of magnitude. The net result was that in the middle stage of the melt period, $K_{f(AOI)}$ was at a seasonal maximum and the transit time through the AOI was

approximately two orders of magnitude lower than in the early and late stages of the melt period. Large variations in soil thaw depth on short distances can result from variations in the disappearance of the snow cover, which can produce large local variations in drainage patterns. These and other observations of the close coupling of soil thaw and drainage led to a new conceptual understanding of drainage from organic-covered permafrost hillslopes that emphasizes the importance of not only the frost table depth but also of the frost table topography. Given that overland flow in these environments is relatively rare, the time and space variable of frost table topography should supersede the ground surface topography as the focus of hillslope runoff models.

ACKNOWLEDGEMENTS

The authors wish to thank C. De Beer, S. McCartney and T. Shirazi for their assistance in the field; Claire Kaufman for her assistance with data preparation and image analysis; G. Ford and R. Janowicz of the Yukon Territorial Government and R. Granger and N. Hedstrom of Environment Canada for providing logistical assistance during the field study; Drs. M. Hayashi and J. Pomeroy for insightful discussion; and L. E. Goodrich, D. W. Riseborough and Yu Zhang for providing the original and modified code of TONE model. This research was funded by the Canadian Foundation for Climate and Atmospheric Sciences and the Natural Science and Engineering Research Council of Canada.

REFERENCES

- Arkin H, Colton RR. 1956. *Statistical Methods*. Barnes & Noble, Inc: New York; 226 p.
- Bayard D, Stähli M, Parriaux A, Flüeler H. 2005. The influence of seasonally frozen soil on the snowmelt runoff at two alpine sites in southern Switzerland. *Journal of Hydrology* **309**: 66–84.
- Beck PSA, Kalmbach E, Joly D, Stien A, Nilsen L. 2005. Modelling local distribution of an Arctic dwarf shrub indicates an important role for remote sensing of snow cover. *Remote Sensing of Environment* **98**: 110–121.
- Carey SK, Quinton WL. 2005. Evaluating runoff generation during summer using hydrometric, stable isotope and hydrochemical methods in a discontinuous permafrost alpine catchment. *Hydrological Processes* **19**: 95–114.
- Carey SK, Woo MK. 1998. Snowmelt hydrology of two subarctic slopes, southern Yukon, Canada. *Nordic Hydrology* **29**: 331–346.
- Carey SK, Woo MK. 2000. Within slope variability of ground heat flux, Subarctic Yukon. *Physical Geography* **21**: 407–417.
- Carey SK, Woo MK. 2001. Slope runoff processes and flow generation in a subarctic, subalpine environment. *Journal of Hydrology* **253**: 110–129.
- Dunne T, Price AG, Colbeck SC. 1976. The generation of runoff from subarctic snowpacks. *Water Resources Research* **12**: 677–685.
- Goodrich LE. 1978. Efficient numerical technique for one dimensional geothermal problems with phase change. *International Journal of Heat and Mass Transfer* **21**: 615–621.
- Goodrich LE. 1982a. *An introductory review of numerical methods for ground thermal regime calculations*. DBR paper No. 1061, Division of Building Research, National Research Council of Canada. Ottawa. 33 p.
- Goodrich LE. 1982b. The influence of snow cover on the ground thermal regime. *Canadian Geotechnical Journal* **19**: 421–432.
- Halliwell DH, Rouse WR. 1987. Soil heat flux in permafrost: characteristics and accuracy of measurement. *Journal of Climatology* **7**: 571–584.
- Hayashi M, Goeller N, Quinton WL, Wright N. 2007. A simple heat-conduction method for simulating frost table depth in hydrological models. *Hydrological Processes* **21**: 2610–2622.
- Hinzman LD, Kane DL, Everett KR. 1993. Hillslope hydrology in an Arctic setting. In *Proceedings, Permafrost, 6th International Conference*, Beijing, 5–9 July, Vol. 1.
- Klene AE, FE Nelson, NI Shiklomanov. 2001. The N-factor in natural landscapes: variability of air and soil-surface temperatures, Kuparuk River basin, Alaska, U.S.A. *Arctic, Antarctic and Alpine Research* **33**: 140–148.
- Kolberg SA, Gottschalk L. 2006. Updating of snow depletion curve with remote sensing data. *Hydrological Processes* **20**: 2363–2380.
- Lewkowicz AG, Ednie M. 2004. Probability mapping of mountain permafrost using the BTS method, Wolf Creek, Yukon Territory, Canada. *Permafrost and Periglacial Processes* **15**: 67–80.
- Lewkowicz AG, French HM. 1982. The hydrology of small runoff plots in an area of continuous permafrost. In *Proceedings of 4th Canadian Permafrost Conference*. National Research Council of Canada: Banks Island, NWT; 151–162.
- Mendenhall W, Beaver RJ, Beaver BM. 1999. *Introduction to Probability and Statistics*, 10th edn. Duxbury Press: New York.
- Nagler T, Rott H, Malcher PM, Müller F. 2008. Assimilation of meteorological and remote sensing data for snowmelt runoff forecasting. *Remote Sensing of Environment* **112**: 1408–1420.
- National Research Council of Canada. 1988. *Glossary of permafrost and related ground-ice terms, permafrost subcommittee, associate committee on geotechnical research*. Technical memorandum No. 142, Ottawa.
- Orlandini S, Perotti A, Sfondrini G, Bianchi A. 1999. On the storm flow response of upland Alpine catchments. *Hydrological Processes* **13**: 549–562.
- Pomeroy JW, Lesack L, Marsh P. 1993. Relocation of major ions in snow along the tundra-taiga ecotone. *Nordic Hydrology* **24**: 151–168.
- Pomeroy JW, Toth B, Granger RJ, Hedstrom NR, Essery RLH. 2003. Variation in surface energetics during snowmelt in a subarctic mountain catchment. *Journal of Hydrometeorology* **4**: 702–719.
- Quinton WL, Carey SK, Goeller NT. 2004. Snowmelt runoff from northern alpine tundra hillslopes: major processes and methods of simulation. *Hydrology and Earth System Sciences* **8**: 877–890.
- Quinton WL, Hayashi M, Carey SK. 2008. Peat hydraulic conductivity in cold regions and its relation to pore size and geometry. *Hydrological Processes* **22**: 2829–2837.
- Quinton WL, Marsh P. 1998. The influence of mineral earth hummocks on subsurface drainage in the continuous permafrost zone. *Permafrost and Periglacial Processes* **9**: 213–228.
- Quinton WL, Pomeroy JW. 2006. Transformations of runoff chemistry in the arctic tundra, Northwest Territories, Canada. *Hydrological Processes* **20**: 2901–2919.
- Quinton WL, Shirazi T, Carey SK, Pomeroy JW. 2005. Soil water storage and active-layer development in a sub-alpine tundra hillslope, southern Yukon Territory, Canada. *Permafrost and Periglacial Process* **16**: 369–382.
- Riseborough DW. 2004. *Exploring the parameters of a simple model of the permafrost-climate relationship*. Unpublished PhD thesis. Carleton University, Ottawa, Canada.
- Rydén BE. 1977. Hydrology of Truelove Lowland. In *Truelove Lowland, Devon Island, Canada: A High Arctic Ecosystem*, Bliss LC (ed). University of Alberta Press: Edmonton; 107–136.
- Salomonson VV, Appel I. 2004. Estimating fractional snow cover from MODIS using the normalised difference snow index. *Remote Sensing of Environment* **89**: 351–360.
- Schaper J, Martinec J, Seidel K. 1999. Distributed mapping of snow and glaciers for improved runoff modelling. *Hydrological Processes* **13**: 2023–2031.
- Slaughter CW, Kane DL. 1979. Hydrologic role of shallow organic soils in cold climates. In *Proceedings, Canadian Hydrology Symposium 79—Cold Climate Hydrology*. National Research Council of Canada: Ottawa; 380–389.
- Stieglitz M, Shaman J, McNamara J, Engel V, Shanley J, Kling G. 2003. An approach to understanding hydrologic connectivity on the hillslope and the implications for nutrient transport. *Global Biogeochemical Cycles* **17**: 1105, DOI:10.1029/2003GB002041.
- Swamy AN, Brivio PN. 1997. Modelling runoff using optical satellite remote sensing data in a high mountainous alpine catchment of Italy. *Hydrological Processes* **11**: 1475–1491.
- Wetzel K.-F. 2003. Runoff production processes in small alpine catchments within the unconsolidated Pleistocene sediments of the Lainbach area (Upper Bavaria). *Hydrological Processes* **17**: 2463–2483.

- Woo M.-K, Arain AM, Mollinga M, Yi S. 2004. A two-directional freeze and thaw algorithm for hydrologic and land surface modelling. *Geophysical Research Letters* **31**: L12501, DOI:10.1029/2004GL019475.
- Wright N, Quinton WL, Hayashi M. 2008. Hillslope runoff from ice-cored peat plateau in a discontinuous permafrost basin, Northwest Territories, Canada. *Hydrological Processes* **22**: 2816–2828.
- Zhang Y, Carey SK, Quinton WL. 2008. Evaluation of the algorithms and parameterizations for ground thawing and freezing simulation in permafrost regions. *Journal of Geophysical Research—Atmospheres* **113**: D17116, DOI:10.1029/2007JD009343.